Computers and Concrete, Vol. 9, No. 4 (2012) 257-273
DOI: http://dx.doi.org/10.12989/cac.2012.9.4.257

The 3D-numerical simulation on failure process of concrete-filled tubular (CFT) stub columns under uniaxial compression

W.C. Zhu*[1], L. Ling[1], C.A. Tang[2], Y.M. Kang[1] and L.M. Xie[1]

[1]*School of Resource and Civil Engineering, Northeastern University, Shenyang 110004, China*
[2]*School of Civil and Hydraulic Engineering, Dalian University of Technology, Dalian, 116024, China*

(Received June 10, 2010, Revised December 24, 2010, Accepted June 22, 2011)

Abstract. Based on the heterogeneous characterization of concrete at mesoscopic level, Realistic Failure Process Analysis (RFPA^{3D}) code is used to simulate the failure process of concrete-filled tubular (CFT) stub columns. The results obtained from the numerical simulations are firstly verified against the existing experimental results. An extensive parametric study is conducted to investigate the effects of different concrete strength on the behaviour and load-bearing capacity of the CFT stub columns. The strength of concrete considered in this study ranges from 30 to 110 MPa. Both the load-bearing capacity and load-displacement curves of CFT columns are evaluated. In particular, the crack propagation during the deformation and failure processes of the columns is predicted and the associated mechanisms related to the increased load-bearing capacity of the columns are clarified. The numerical results indicate that there are two mechanisms controlling the failure of the CFT columns. For the CFT columns with the lower concrete strength, they damage when the steel tube yields at first. By contrast, for the columns with high concrete strength it is the damage of concrete that controls the overall loading capacity of the CFT columns. The simulation results also demonstrate that RFPA^{3D} is not only a useful and effective tool to simulate the concrete-filled steel tubular columns, but also a valuable reference for the practice of engineering design.

Keywords: concrete-filled tubular (CFT) stub column; load-bearing capacity; failure process; heterogeneity; numerical simulation.

1. Introduction

In modern structural constructions, concrete-filled steel tube columns have gradually become a central element in structural systems like tall buildings, bridges and so on. Their usage provides high strength, high ductility, high stiffness and full usage of construction materials. In addition to these advantages, the steel tubes surrounding the concrete columns eliminate temporarily formwork which reduces construction time, assisting in carrying axial load and providing confinement to the concrete.

Experimentally, considerable research efforts have been made to identify the strength and behaviour of concrete-filled steel tube columns. Tests of concrete-filled steel tube columns were conducted by Liu *et al.* (2003), Uy (2001), Schneider (1998), Han and Yao (2003), Sakino *et al.* (2004) and many other researchers. These tests were carried out on concrete-filled mild steel and high strength steel tube columns using circular, square and rectangular hollow sections. In addition, Yang and Han

* Corresponding author, Professor, E-mail: zhuwancheng@mail.neu.edu.cn

(2006) tested the behaviour of hollow structural steel (HSS) stub columns and beams filled with normal concrete and recycled aggregate concrete (RAC) under instantaneous loading.

In order to understand the behaviour and the failure mechanisms of concrete-filled steel tube (CFST) columns, numerical modeling has been widely used, too. Schneider (1998) used the ABAQUS program to develop a 3D nonlinear finite element model for concrete-filled steel tube circular columns. Hu *et al.* (2003) developed a nonlinear finite element (FE) model using the ABAQUS program to simulate the behaviour of CFT columns. The concrete confinement was achieved by matching the numerical results by trial and error via parametric study. Uy (1998) used the finite strip method to analyze the cross-section. The effect of width to thickness ratio on the strength capacity of in-filled composite columns has been highlighted. Hu *et al.* (2005) proposed the material constitutive models for concrete-filled tube (CFT) columns subjected to an axial compressive force and predicted the mechanical behavior of CFT columns. By using non-linear finite element analysis with the general purpose finite element package ABAQUS, Xiong and Zha (2007) investigated the behaviour of CFST columns under initial stresses. Huang *et al.* (2008) proposed a model to estimate the ultimate strength of rectangular concrete-filled steel tubular (CFT) stub columns under axial compression, in which the ultimate strength of concrete core is determined by using the conception of the effective lateral confining pressure and a failure criterion of concrete under true triaxial compression. Starossek *et al.* (2010) developed the nonlinear finite element models to study the force transfer between steel tube and concrete core under three types of loading, where the ABAQUS was used to simulate the concrete material behavior. Liang (2011) also presented a new numerical model to predict the nonlinear inelastic behaviour of high strength circular concrete-filled steel tubular slender beam-columns.

The behaviour of concrete-filled steel tube columns has been studied in detail for decades either by experiment or by numerical analysis and many scientific achievements have been made. However, the majority of these numerical investigation are focused on prediction of the load-displacement behavior of the CFT columns using the finite element method; in this regard, the details of the failure mechanisms, including the initiation, propagation, coalescence of microcracks etc. are not fully understood and still remain the subject of considerable scientific interest. Due to the heterogeneity of concrete, it is difficult to study the deformation and failure process of CFT columns by using theoretical analysis. But a numerical tool incorporating the failure process simulation of heterogeneous materials is capable of understanding the mechanical behaviour of CFT columns.

In this paper, Realistic Failure Process Analysis (RFPA^{3D}) code is used to simulate the fracture process of the CFT stub columns subjected to uniaxial loading. The main objective of this study is to present a three-dimensional model established to simulate the influence of the different concrete strength on the behaviour of CFT stub columns and make it clear for us to understand the crack propagation in heterogeneous materials.

2. Numerical model

2.1 Brief introduction of RFPA^{3D}

The RFPA^{3D} code (Tang 1997) can be used for modeling the evolution of damage or crack initiation, propagation and coalescence in brittle material. The solid or structure is assumed to be composed of many mesoscopic elements with the same size, and the mechanical properties of these elements are assumed to conform to a given Weibull distribution as defined in the following probability density function (pdf)

$$f(u)=\frac{m}{u_0}\left(\frac{u}{u_0}\right)^{m-1}\exp\left(-\left(\frac{u}{u_0}\right)^{m}\right) \tag{1}$$

where u is the mechanical parameter of the element (such as strength or elastic modulus); the scale parameter u_0 is related to the average of the element parameters and the parameter m defines the shape of the distribution function. From the properties of the Weibull distribution, a larger value of m implies a more heterogeneous material and vice versa. Therefore, the parameter m is called the homogeneity index in RFPA^{3D}. For higher values of the homogeneity index, the strengths of more elements are concentrated closer to u_0. In the definition of the Weibull distribution, the value of the parameter m must be larger than 1.0. Using the pdf, in a computer simulation of a medium composed of many mesoscopic elements, one can produce numerically a heterogeneous material. The computationally produced heterogeneous medium is analogous to a real specimen tested in the laboratory, so in this investigation it is referred to as a numerical specimen. In general, it has been assumed that the Young's modulus and the strength of the mesoscopic elements that is used to simulate a rock specimen conform to two individual distributions with the same heterogeneity index. The mesoscopic elements themselves are isotropic and homogeneous. The elements in the specimen must be sufficiently small to reflect the heterogeneous mechanical properties of materials at the meso-scale and still provide conditions under which a current computer can perform the analysis efficiently. In general, the homogeneity index and other Weibull distribution parameters are specified based on that the numerical specimen can not only fit the material properties (including Young's modulus and strength), but also reproduce the stress-strain curve of the real concrete specimen. In this study, the homogeneity index m of 3.0 is specified for the strength and elastic modulus of concrete, while that of steel equals to 200.

The Weibull distribution parameters of numerical specimen of concrete are chosen so as to simulate the actual behaviour of concrete. The Weibull distribution parameters of the strength and elastic modulus of concrete used in RFPA^{3D} simulation are fitted according to the following Eqs. (2) and (3) (Zhu *et al.* 2004, Liang *et al.* 2006)

$$\frac{f_{cs}}{f_{cs0}}=0.2047\ln(m)+0.1156 \tag{2}$$

$$\frac{E_s}{E_{s0}}=0.0813\ln(m)+0.7679 \tag{3}$$

where f_{cs} and E_s are strength and elastic modulus of the concrete that will be simulated; f_{cs0} and E_{s0} are mean strength and elastic modulus of the Weibull distribution used to simulate the concrete.

Initially an element is considered elastic, with elastic properties defined by Young's modulus and Poisson's ratio. The stress-strain relation for an element is considered linear elastic until the given damage threshold is attained, and then is modified by softening. Acoustic emission studies have shown that the process of cracking cannot be represented either by tensile crack opening alone or by crack sliding alone (Meglis *et al.* 1995). Mechanisms consisting of tensile-opening and shearing seem to be dominant in comparison with other mechanisms of crack evolution (Hoxha and Homand 2000). Therefore, in RFPA^{3D}, damage of elements in tension or shear is initiated when its state of stress satisfies the maximum tensile stress criterion or the Mohr-Coulomb criterion, respectively, in order to capture the principal modes of damage in concrete. Because microscopic fracture is the fundamental damage process, the tensile strain criterion is applied preferentially.

In elastic damage mechanics, the elastic modulus of an element degrades monotonically as damage evolves, and the elastic modulus of damaged material is expressed as follows (Zhu and Tang 2002, Zhu and Tang 2004, Zhu *et al.* 2004).

$$E = (1-D)E_0 \tag{4}$$

where D represents the damage variable, and E and E_0 are the elastic moduli of the damaged and the undamaged material, respectively. In the current method, the element as well as its damage is assumed isotropic, so the E, E_0 and D are all scalar.

The sign convention used throughout this paper is that compressive stress and strain are positive. When the mesoscopic element is in a uniaxial stress state (both uniaxial compression and uniaxial tension), the constitutive relation of elements is as illustrated in Fig. 1. Initially, the stress-strain curve is linear elastic and no damage exists, i.e., $D = 0$.

As shown in Fig. 1, when the maximum tensile principal stress in an element reaches its tensile strength f_{t0}, that is

$$\sigma_3 \le -f_t\,, \tag{5}$$

the damage variable can be described as

$$D = \begin{cases} 0 & \varepsilon_{t0} \le \varepsilon \\ 1-\dfrac{f_{tr}}{E_0\varepsilon} & \varepsilon_{tu} \le \varepsilon < \varepsilon_{t0} \\ 1 & \varepsilon \le \varepsilon_{tu} \end{cases} \tag{6}$$

where f_{tr} is the residual tensile strength. Other parameters in the equation are defined in Fig. 1.

In order to study the damage of an element when it is under compressive and shear stress, the Mohr-Coulomb criterion, expressed as follows, is chosen to define the second damage threshold.

$$\sigma_1 - \frac{1+\sin\varphi}{1-\sin\varphi}\sigma_3 \ge f_{c0} \tag{7}$$

where φ is the internal friction angle and f_{c0} is the uniaxial compressive strength. The damage

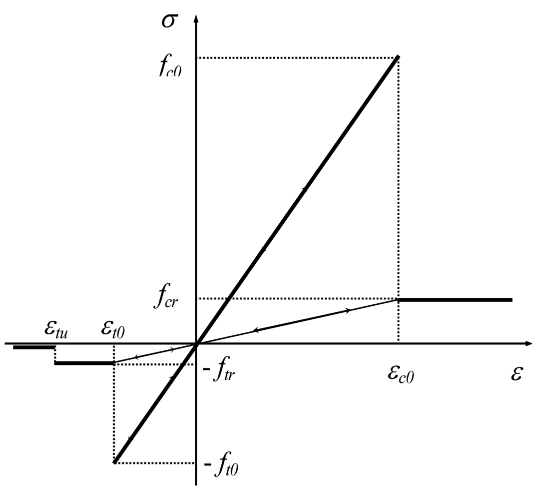

Fig. 1 Elastic constitutive law of concrete subjected to uniaxial stress

variable under uniaxial compression is described as

$$D = \begin{cases} 0 & \varepsilon < \varepsilon_{c0} \\ 1 - \dfrac{f_{cr}}{E_0 \varepsilon} & \varepsilon_{c0} \le \varepsilon \end{cases} \tag{8}$$

where f_{cr} is the residual compressive strength.

When Eqs. (5)-(8) are extended to three dimensional cases, we can use the maximum principal strain ε_3 to replace the tensile strain ε in Eq. (6) and ε_1 to replace the tensile strain ε in Eq. (8), respectively. As presented above, the concrete is simulated as the elastic-brittle material with a residual strength, however its residual strength may increase with the confining stress. The steel is simulated as the elastic-plastic material. In this regard, the confinement of steel tube may apply confining stress on the concrete specimen, thus raising the loading capacity of CFT stub columns. More detailed descriptions about the constitutive law of elements have been presented elsewhere (Zhu and Tang 2002, Zhu *et al.* 2004, Liang *et al.* 2006).

2.2 Constitutive relations of the steel tubes

In this study, the steel is considered to be homogeneous and is simulated as an ideal elastoplastic material with a Young's modulus of 210 GPa and a Poisson's ratio of 0.3. The simple stress-strain relation is in the following form (see Fig. 2)

$$\sigma_s = \begin{cases} f_{sy} & \varepsilon_{sy} \le \varepsilon_s \\ \varepsilon_s E_s & -\varepsilon_{sy} \le \varepsilon_s \le \varepsilon_{sy} \\ -f_{sy} & \varepsilon_s < -\varepsilon_{sy} \end{cases} \tag{9}$$

where σ_s and ε_s are stress and strain of steel, and f_{sy}, E_s and ε_{sy} are the yield stress, the elastic modulus and the yield strain of steel, respectively.

3. Verification of numerical model

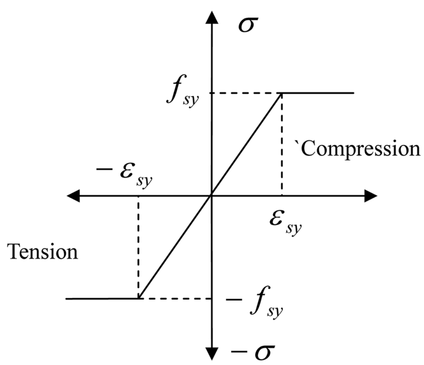

Fig. 2 The constitutive law of the steel

Table 1 Comparison between the numerical and experimental results

Specimen	Dimensions				Material properties		Ultimate load / KN		Ratio between the numerical and experiment ultimate load
	D/mm	*t*/m	*D*/*t*	*L*/mm	Strength of concrete /MPa	Strength of steel /MPa	Numerical results with RFPA^{3D}	Experimental results by other researchers	
*C*7	115.0	4.91	23.4	300.5	34.7	365	1432.0	1380 (Giakoumelis and Lam 2004)	1.04
*C*8	115.0	4.92	23.4	300.0	104.9	365	1861.5	1787 (Giakoumelis and Lam 2004)	1.05
*C*9	115.0	5.02	22.9	300.5	57.6	365	1476.6	1413 (Giakoumelis and Lam 2004)	1.05
*C*11	114.29	3.75	30.5	300.0	57.6	343	1136	1067 (Giakoumelis and Lam 2004)	1.06
*C*12	114.3	3.85	29.7	300.0	31.9	343	1017	998 (Giakoumelis and Lam 2004)	1.02
*C*14	114.5	3.84	29.8	300.0	98.9	343	1454.3	1359 (Giakoumelis and Lam 2004)	1.07
11	133.2	5.06	26.3	397.0	46.5	351	1672.7	1580 (Zhang and Wang 2004)	1.06
29	160.2	5.01	32.0	476.0	77.1	356.3	2296.0	2440 (Zhang and Wang 2004)	0.94
33	131.1	5.04	26.0	397.0	77.1	351	1979.5	1955 (Zhang and Wang 2004)	1.01

Giakoumelis and Lam (2004), Zhang and Wang (2004)

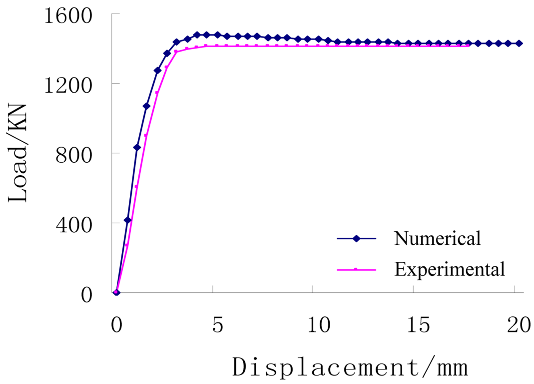

Fig. 3 Comparison of load-displacement curves with experimental results for specimen *C*9 conducted by Giakoumelis and Lam (2004)

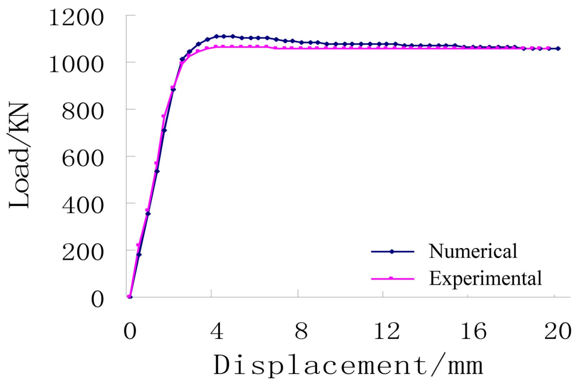

Fig. 4 Comparison of load-displacement curves with experimental results of for specimen *C*11 conducted by Giakoumelis and Lam (2004)

The validation of RFPA^{3D} for triaxial tests and acoustic emission characteristics of concrete and rock was given in previous publications (such as Zhu *et al.* 2004, Zhu and Tang 2004, Liang *et al.* 2006). In this section, the RFPA^{3D} is validated by simulating the experimental results from Giakoumelis and Lam (2004) and Zhang and Wang (2004). For the failure process of concrete, which is the distinct feature of RFPA^{3D} from other conventional finite element package, because it can not be observed during the experiments of CFT stub columns, it is difficult to use to validate the RFPA^{3D}. Therefore, the RFPA^{3D} is used to predict the load-deformation curves of several CFT stub columns, and it is validated by comparing the numerical results with the experimental ones.

The same models and mechanical parameters are selected from other references (Giakoumelis and Lam 2004, Zhang and Wang 2004). The specimen geometry and dimensions are listed in Table 1. The material properties for the concrete, steel tubes are adopted based on the experimental data (Zhang and Wang 2004).

Table 1 shows the ultimate loads obtained from the experiments and those calculated with RFPA^{3D}. A maximum difference of 7% is observed between the simulation results and the experimental observation for column *C*14. Fig. 3 and Fig. 4 show the experimental load-displacement curves of the specimen *C*9 and *C*11. It can be seen that the simulation results agree well with the experiment observation. For the other specimens, the similar curves are given, and therefore they are omitted in the paper. This illustrates that RFPA^{3D} code is effective in simulating the mechanical behavior of CFT stub columns.

4. Application of model and discussion

4.1 Model setup

In order to study the influence of concrete strength on the behaviour of the CFT stub columns, in this section, the specimens of CFT stub columns with different concrete strength are numerically simulated. The strength of concrete considered in this study is 30, 50, 70, 90 and 110 MPa, respectively. The geometry and material properties of the specimens are summarized in Table 2. All five specimens (numbered as *A*1-*A*5) are discretized into 166400 uniform 8-node iso-parametric elements and the elastic modulus and strength of the elements are assumed to conform to Weibull distribution. Scale parameters of elastic modulus and compressive strength are listed in Table 3. It is important to note that, for the particular parameters used in the Weibull distribution, if a numerical specimen of rock with a size of 100 mm × 100 mm is constructed of elements with a mean strength of 97 MPa, the global compressive strength realized in the model is only 30 MPa. Only when the homogeneity index tends to infinity (when the specimen tends to be homogeneous) would the numerically simulated strength be close to the given mean strength of elements (Zhu and Tang 2002, Zhu and Tang 2004, Liang *et al.* 2006). More detailed explanations about this phenomenon have been given in previous papers (Zhu and Tang 2004, Zhu *et al.* 2004, Liang *et al.* 2006). This can explain why the average strengths given in Table 3 are much larger than those for real concrete.

In this simulation, the specimens are under uniaxial compression in vertical direction, and a displacement of 0.02 mm is applied vertically step by step at the top surface of the specimen, while the bottom surface of the specimen is fixed from the vertical movement.

4.2 Effect of concrete strength on loading capacity

Table 2 summarizes the maximum loads of all the specimens, where the maximum applied axial force is denoted by P_{max}. From the Table 2, it can be seen that the ultimate loads of CFT stub columns increase with the increasing concrete strength, but the increment rate of P_{max} slows down with the concrete strength.

The load-displacement curves of all the specimens are also obtained by RFPA^{3D} and shown in

Table 2 Geometry, material properties and the simulation results

Specimen	Dimensions			Material properties		Ultimate load/ KN	Increment of strength of the CFT stub columns
	D/mm	t/mm	L/mm	Concrete f_c/ MPa	Steel f_y/MPa	P_{max}	(%)
*A*1	115.0	3	300.0	30	345	813.6	0.00
*A*2	115.0	3	300.0	50	345	1010.5	24.2
*A*3	115.0	3	300.0	70	345	1200.3	18.7
*A*4	115.0	3	300.0	90	345	1367.9	13.9
*A*5	115.0	3	300.0	110	345	1529.2	11.7

Table 3 Weibull distribution parameters of the concrete and steel tube

Specimen	Homogeneity index	Scale parameter of elastic modulus/GPa	Scale parameter of compressive strength/MPa
*A*1	3	29.7	97
*A*2	3	38.4	161
*A*3	3	47.6	226
*A*4	3	54	290
*A*5	3	59.7	355
Steel tube	200	210	345

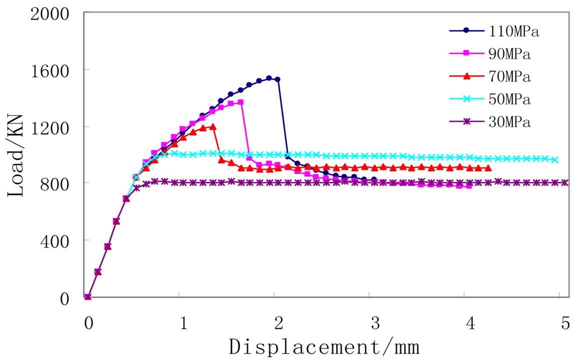

Fig. 5 Load-displacement curves of CFT columns with different concrete strength

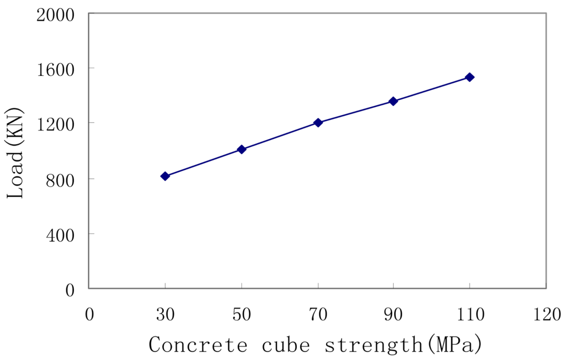

Fig. 6 The relationship between the strength of CFT columns and that of concrete

Fig. 5. Because in RFPA^{3D} the whole structure is elastic when there is no element damaged, the damage of some elements may make the macroscopic load-displacement curve of specimen deviate from linearity. Seeing from the load-displacement curves, we can find that the inelasticity occurs in each specimen when the applied load attains 70%~80% of P_{max} during the whole loading process. It is obvious that when the concrete strength increases, the load-bearing capacity of CFT stub columns is improved, too, and however the columns become brittle. The simulation results show that the lower concrete strength yields an earlier onset of non-linear behavior and the smaller magnitude of P_{max}, while high concrete strength yield the longer linear behavior. It can be also found that the load-displacement curves follow a load drop when the axial load of column reaches its peak. And also, this load drop becomes more evident as the increase of concrete strength.

As shown in Fig. 6, the effect of concrete strength on the load-bearing capacity (P_{max}) of the CFT stub columns is seen to be linear, i.e., the loading capacity of CFT stub columns (P_{max}) increases approximately linearly with the concrete strength. Based on these simulations, it can be concluded that the concrete strength has a significant influence on the load-displacement response and strength characterization of CFT stub columns.

4.3 Influence of concrete strength on microfracture behavior

The monitoring of acoustic emission (AE) activities during the deformation is one of the well-known measures to characterize the internal damage of concrete. Thus, AE technique has been employed for many years to study damage and microcrack nucleation in concrete materials (Berthelot and Rovert 1987). In RFPA^{3D}, every damaged element is considered to be a source of acoustic event since the damaged element must release its elastic energy stored during their deformation. Therefore, by recording the number of failed elements and the associated amount of energy release, RFPA^{3D} is capable of simulating the AE activities including the AE event rate, magnitude and their locations during the failure process of materials. In the numerical simulations of concrete failure, the AE distributions are used to indicate the locations of damage initiation and the paths of crack propagation during the failure process.

As shown in Fig. 7, the numerical results demonstrate that the AE (acoustic emission) event patterns of the CFT stub columns are greatly affected by the concrete strength. Fig. 7(a) shows AE count rate as a function of deformation for the five CFT stub columns with different concrete

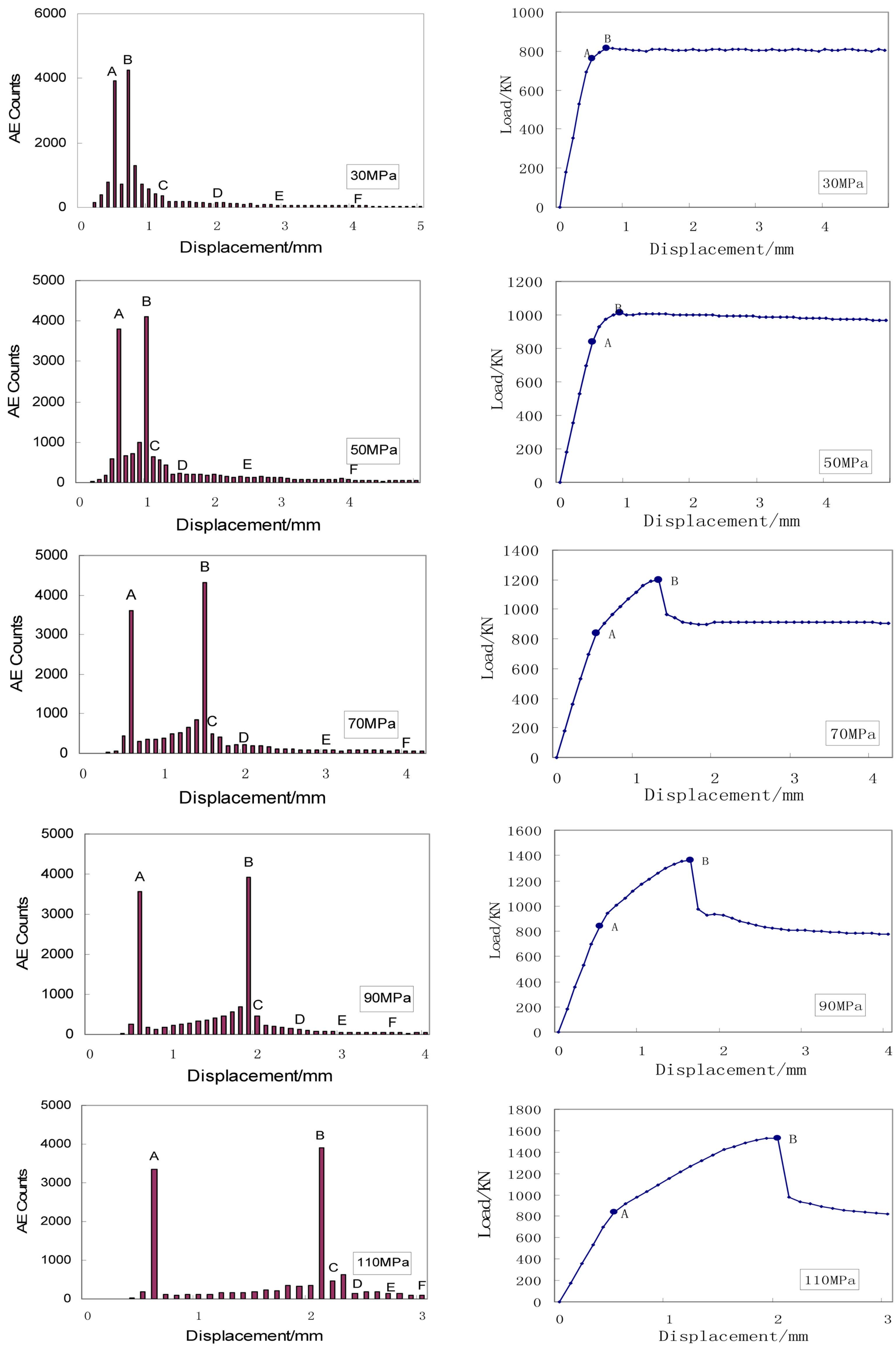

(a) AE patterns (b) Load-displacement curve

Fig. 7 AE patterns and load-displacement curves of the CFT columns with different strength of concrete strength. It can be seen that a large number of AE events occurred before reaching the peak load for these five specimens. However, the specimens with relatively low concrete strength emit more AE events as the precursory of macro-fracture than those of the relatively high concrete strength. On the other hand, higher stress drop is observed to be correspondent to the higher event rate in the specimen of relatively high concrete strength. Fig. 7 shows a similar trend between the modeled load-displacement curves and the modeled curves of event rate.

It is important to find that the highest AE event counts do not correspond to the maximal load, but to the condition just after the peak load. This phenomenon is attributed to a large amount of deformation energy released at this moment. Even if the maximum load of the specimen is exceeded, the micro-failure continues to occur. This kind of strong correlation between AE activity and inelastic deformation can be used as an indicator to evaluate the damage accumulation in concrete structure.

As shown in Fig. 7(b), the load-displacement curve is approximately linear before point A; correspondingly, there is no AE in the CFT stub columns. And then the stress of steel tube reached point A, at this stage, although there is no acoustic emission in the concrete (stage a in Fig. 9 and 10), some failed elements are found in the steel tube (see point A in Fig. 7(a)). After that, the load gradually increased up to $P_{\max}$ (point B) where the load-displacement curve is tortuous, exhibiting non-linear response due to the yielding of the steel tubes and damage of the concrete. Some macro cracking developed in the concrete by the end of the elastic range, and when the load reaches point (B), the cracks grow abruptly, which results in occurrence of large number of microfractures (after point B in Fig. 7). Therefore, the failure of the steel tube is also closely related to the concrete strength. This can be made clear when we compare Figs. 7(a) and (b). It can be also seen that the number of failed elements in the steel tube decreases with the increasing of the concrete strength.

Fig. 8 shows the cumulative AE events as a function of deformation. The results show that the relatively high concrete strength specimen emits more AE energy as the precursory of macro-fracture than that of the relatively low concrete strength specimen. Comparing Fig. 7(a) with Fig. 8, it can be seen that during the initial deformation stage, little elastic energy is released, although more than 50% of the AE events occurred before reaching the peak load, less than 20% of the acoustic energy is dissipated during this stage. Comparing Fig. 5 and Figs. 7 with Fig. 8, it must be noted that every large load drop in the load-displacement curve as shown in Fig. 5 corresponds to a high event rate in Fig. 7 and large event energy release in Fig. 8.

In Fig. 9, we present the locations of AE events occurring during the failure process of CFT stub

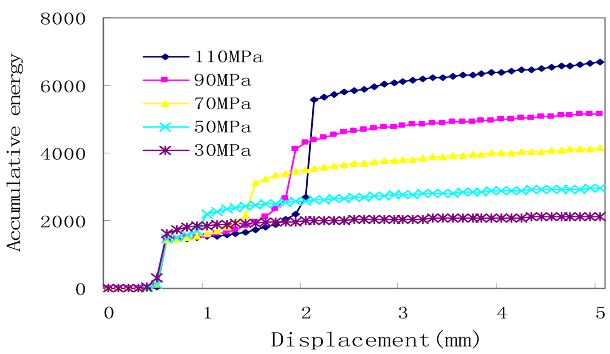

Fig. 8 Accumulated energy release for different CFT columns

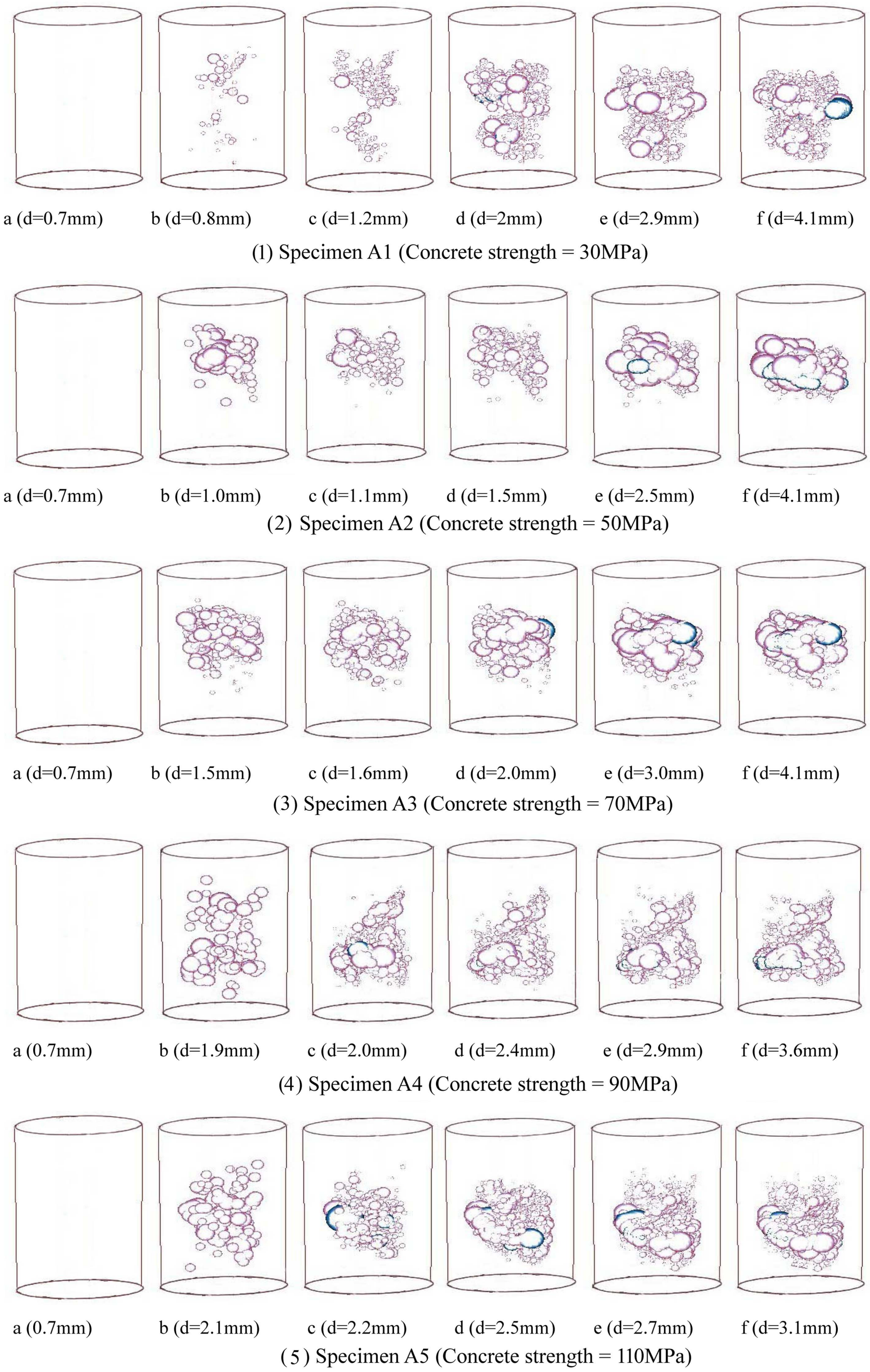

Fig. 9 AE distribution of CFT columns with the different concrete strength (*d* is the applied axial displacement)

columns, from which, the failure mechanisms controlled by tensile or shear damages can be distinguished. This kind of analysis is helpful in understanding the interaction between concrete specimen and steel tube during the whole failure process of CFT stub columns. Each sphere represents one AE event and the diameter of the circle represents the relative magnitude of the AE released energy. In the pictures, the pink red circles represent the AE due to shear damage, while the dark blue circle represent the AE from tensile damage. It can be found that tensile failures dominate in the specimens of relatively low concrete strength and the combination of tensile failures and some shear failures exists in the specimens of relatively high concrete strength. This is because that the confinement of steel tube is more prominent when the strength of concrete is relatively high.

Thereafter, it can be concluded that two mechanisms controlling the failure of the CFT stub columns. For the CFT stub columns with the lower concrete strength, they fail when the steel tube yields at first. By contrast, for the columns with high concrete strength it is the damage of concrete that controls the overall loading capacity of the CFT stub columns. Of course, under any circumstances, both the damage in CFT stub columns and the enhancement of loading capacity are closed related to the passive confinement applied by the steel tube.

4.4 Influence of concrete strength on failure modes

From the final exterior failure pattern of five specimens, as shown in Fig. 10, the lateral dilation of five CFT stub columns are vividly simulated, which is phenomenally similar to the experiment observations. However, as usually observed in the experiments, no apparent difference is found for this exterior failure pattern of CFT stub columns under different core concrete strength, therefore, further clarification on the failure mechanism based on the internal failure mode is really required.

In Fig. 11, the stress distribution at the vertical slice along the center of the CFT stub columns during the failure process is shown. In this figure, the shade of grey displays the relative magnitude of maximum principal stress. Since the damaged elements may have a lower stress, from this figure, the initiation, propagation and coalescence of the cracks during the loading process are observed. The following stages are observed during the progressive failure process of five specimens:

(1) During the initial loading stage, no cracks are localized in the five specimens (see stage (a) in Fig. 11). The load-displacement behavior is nearly elastic (as shown in Fig. 5).

(2) After that, the damaged elements are dispersedly distributed, and they are not connected with each other to form macroscopic cracks (stage b as shown in Fig. 11), although the load-displacement behavior becomes obviously non-linear at this stage (as shown in Fig. 5).

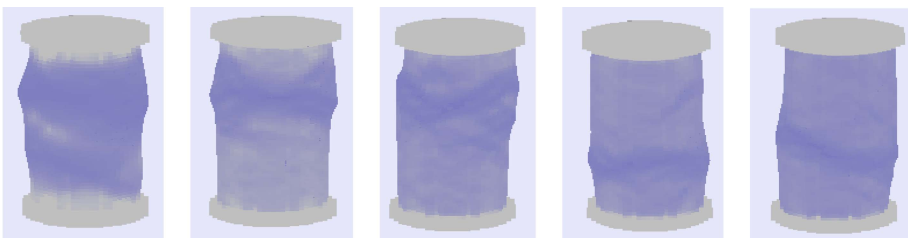

A1 A2 A3 A4 A5

Fig. 10 Exterior failure pattern of CFT columns

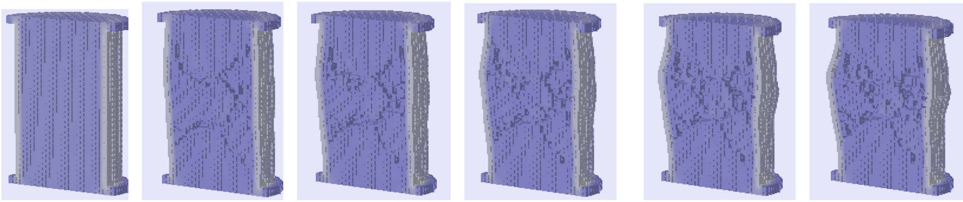

a (d=0.7mm) b (d=0.8mm) c (d=1.2mm) d (d=2mm) e (d=2.9mm) f (d=4.1mm)

(1) Specimen A1 (Concrete strength = 30MPa)

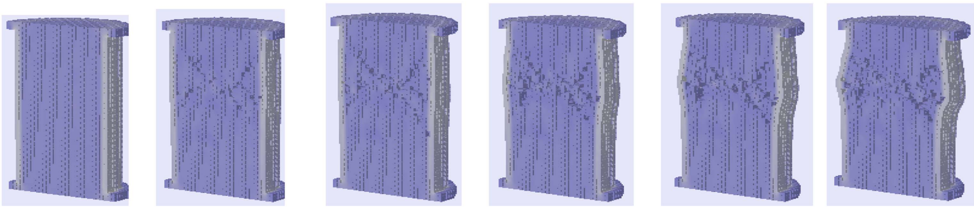

a (d=0.7mm) b (d=1.0mm) c (d=1.1mm) d (d=1.5mm) e (d=2.5mm) f (d=4.1mm)

(2) Specimen A2 (Concrete strength = 50MPa)

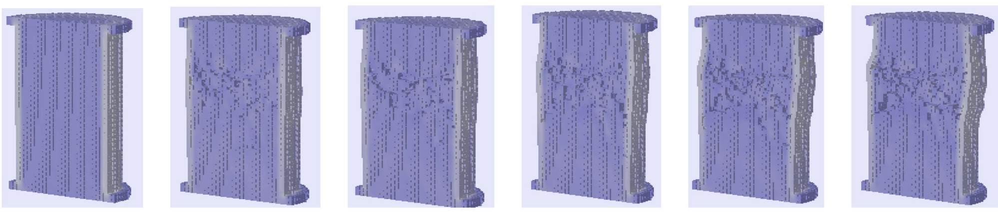

a (d=0.7mm) b (d=1.5mm) c (d=1.6mm) d (d=2.0mm) e (d=3.0mm) f (d=4.1mm)

(3) Specimen A1 (Concrete strength = 70MPa)

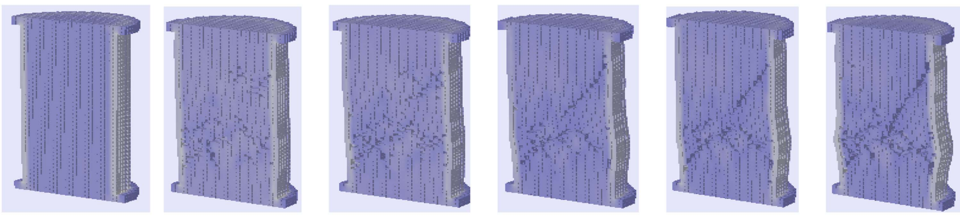

a (0.7mm) b (d=1.9mm) c (d=2.0mm) d (d=2.4mm) e (d=2.9mm) f (d=3.6mm)

(4) Specimen A4 (Concrete strength = 90MPa)

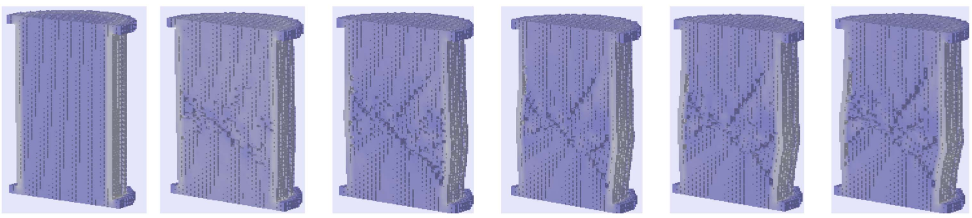

a (0.7mm) b (d=2.1mm) c (d=2.2mm) d (d=2.5mm) e (d=2.7mm) f (d = 3.1mm)

(5) Specimen A5 (Concrete strength = 110MPa)

Fig. 11 Failure process of CFT columns with the different concrete strength (*d* is the applied axial displacement)

(3) As damage accumulates, cracks become clustered, involving more elements and leading to fracture interaction (stage c in Fig. 11). A large load drop during this stage is found (as shown in Fig. 5).

(4) A large number of elements are damaged in the tensile mode at the same step, and a great amount of energy is released, leading to a sharp decrease of the load-carrying capacity of the specimens. Finally, the damaged zones grow further to form macroscopic cracks. As a result, the further damage is induced around the macroscopic cracks at the stage (f).

In general, for the CFT stub columns with low strength concrete their distribution of damages is localized in a region (for example, A1 and A2, with the concrete strength of 30 MPa and 50 MPa, respectively), while the shear bands are formed in a degree of 45° with the vertical loading direction for the specimen with high concrete strength (for example, A4 and A5). Therefore, it is important to note that shear failures dominate in the failure process with the increasing concrete strength.

5. Conclusions

The concrete-filled steel tube columns have plenty of advantages; they have been increasingly used in many modern structures. Obviously, the investigation of structure failure in concrete-filled steel tube columns is of great importance in associated structure mechanics and engineering areas. In the past, the majority of the numerical analysis was developed to predict the load-carrying capacity of CFT column; however, there still fall short of the numerical simulation that can clarify the failure mechanism during the failure process of CFT columns. Therefore it is important to identify the main failure mechanisms associated with damage under external loading. In this study, the RFPA^{3D} code is used to simulate the failure of the CFT stub columns, and the effect of concrete strength on the failure process of CFT stub columns is analyzed. The numerical model is successful in representing cracking pattern and the load-displacement response of CFT stub columns. From the simulation results, the following conclusions are drawn:

(1) Two mechanisms controlling the failure of the CFT stub columns are captured based on the simulations of RFPA^{3D}. For the CFT stub columns with the lower concrete strength, they fail when the steel tube yields at first. By contrast, for the columns with high concrete strength it is the damage of concrete that controls the overall loading capacity of the CFT stub columns.

(2) The load-bearing capacity of CFT stub columns is improved and the ductility of the columns is decreased as the concrete strength increases. The lower concrete strength yields an earlier onset of non-linear behavior and the lower loading capacity, while high concrete strength yields the delayed nonlinearity before the peak load. The specimen of relatively low concrete strength emits more AE events as the precursory of macro-fracture than that of the relatively high concrete strength. The number of failed elements of the steel tube decreases with the increasing of the concrete strength.

(3) Failure behavior of CFT stub columns is influenced by the strength of concrete. Tensile failures dominate in the columns with low concrete strength while the combination of tensile failures and some shear failures exists in the columns with high concrete strength. The numerical code RFPA^{3D} is successful in representing cracking pattern and the load-displacement responses of CFT stub columns.

However, it should be noted that, due to the limit of the computing capacity, although the concrete is assumed as a heterogonous material, the real internal structure characteristics of concrete are not incorporated into the numerical model. Moreover, no special interfacial elements are employed to simulate the interaction between concrete and steel tube. In future, the numerical simulations based on parallel computing will be implemented, and the interface elements will be included, in order to provide more detailed characterization on the failure process of CFT columns.

Acknowledgements

The support from National Science Foundation of China (Grant Nos. 51111130206 and 50934006), the Fok Ying Tung Education Foundation (Grant No. 122023), and the Fundamental Research Funds for the Central Universities of China (Grant Nos. N110201001, N100701001 and N100401001) is greatly appreciated. The authors are grateful to the reviewers for discerning comments on this paper.

References

Berthelot, J. and Rovert, J. (1987), “Modeling concrete damage by acous. emission”, *J. Acous. Emission*, **6**, 43-60.

Ellobody, E., Young, B. and Lam, D. (2006), “Behaviour of normal and high strength concrete-filled compact steel tube circular stub columns”, *J. Constr. Steel Res.*, **62**(7), 706-715.

Giakoumelis, G. and Lam, D. (2004), “Axial capacity of circular concrete-filled tube columns”, *J. Constr. Steel Res.*, **60**(7), 1049-1068.

Han, L.H. and Yao, G.H. (2003), “Influence of concrete compaction on the strength of concrete-filled steel RHS columns”, *J. Constr. Steel Res.*, **59**(6), 751-767.

Hoxha, D. and Homand, F. (2000), “Microstructural approach in damage modelling”, *Mech. Mater.*, **32**(6), 377-387.

Hu, H.T., Huang, C.H., Wu, M.H. and Wu, Y.M. (2003), “Nonlinear analysis of axially loaded concrete-filled tube columns with confinement effect”, *J. Struct. Eng.-ASCE,* **129**(10), 1322-1329.

Huang, Y.S., Long, Y.L. and Cai, J. (2008), “Ultimate strength of rectangular concrete-filled steel tubular (CFT) stub columns under axial compression”, *Steel Compos. Struct.*, **8**(2), 115-128.

Liang, Q.Q. (2011), “High strength circular concrete-filled steel tubular slender beam-columns, Part I: Numerical analysis”, *J. Constr. Steel Res.*, **67**(2), 164-171.

Liang, Z.Z., Tang, C.A., Zhang, Y.B., Ma, T.H. and Zhang, Y.F. (2006), “3D numerical simulation of failure process of rock (in Chinese)”, *Chinese J. Rock Mech. Eng.,* **25**(5), 931-936.

Liu, D., Gho, W.M. and Yuan, J. (2003), “Ultimate capacity of high-strength rectangular concrete-filled steel hollow section stub columns”, *J. Constr. Steel Res.*, **59**(12), 1499-1515.

Meglis, I.L., Chow, T.M. and Young, R.P. (1995), “Progressive microcrack development in test on Lac du Bonnet: I. Emission Source location and velocity measurements”, *Int. J. Rock Mech. Min.*, **32**(8), 741-750.

Sakino, K., Nakahara, H., Morino, S. and Nishiyama, I. (2004), “Behavior of centrally loaded concrete-filled steel-tube short columns”, *J. Struct. Eng.-ASCE*, **130**(2), 180-188.

Schneider, S.P. (1998), “Axially loaded concrete-filled tubes”, *J. Struct. Eng.-ASCE*, **124**(10), 1125-1138.

Starossek, U., Falah, N. and Lohning, T. (2010), “Numerical analyses of the force transfer in concrete-filled steel tube columns”, *Struct. Eng. Mech.*, **35**(2), 241-256.

Tang, C.A. (1997), “Numerical simulation on progressive failure leading to collapse and associated seismicity”, *Int. J. Rock Mech. Min.*, **34**(2), 249-261.

Uy, B. (1998), “Local and post-local buckling of concrete-filled steel welded box columns”, *J. Constr. Steel Res.*, **47**(1-2), 47-72.

Uy, B. (2001), “Strength of short concrete-filled high strength steel box columns”*, J. Constr. Steel Res.*, **57**(2), 113-134.

Yang, Y.F. and Han, L.H. (2006), “Compressive and flexural behaviour of recycled aggregate concrete filled steel

tubes (RACFST) under short-term loadings", *Steel Compos. Struct.*, **6**(3), 257-284.
Zhang, S. and Wang, Y. (2004), "Failure modes of short columns of high-strength concrete-filled steel tubes (in Chinese)", *J. Civil Eng.*, **37**(9), 1-10.
Zhu, W.C. and Tang, C.A. (2002), "Numerical simulation on shear fracture process of concrete using mesoscopic mechanical model", *Constr. Build. Mater.*, **16**(8), 453-463.
Zhu, W.C. and Tang, C.A. (2004), "Micromechanical model for simulating the fracture process of rock", Rock *Mech. Rock Eng.,* **37**(1), 25-56.
Zhu, W.C., Teng, J.G. and Tang, C.A. (2004), "Mesomechanical model for concrete-part I: model development", *Mag. Concrete Res*., **56**(6), 313-330.

CC